

Graphene's morphology and electronic properties from discrete differential geometry

Alejandro A. Pacheco Sanjuan,¹ Zhengfei Wang,²

Hamed Pour Imani,³ Mihajlo Vanević,⁴ and Salvador Barraza-Lopez³

1. *Departamento de Ingeniería Mecánica. Universidad del Norte. Km. 5 Vía Puerto Colombia. Barranquilla, Colombia*

2. *Department of Materials Science. University of Utah. Salt Lake City, UT 84112, USA*

3. *Department of Physics. University of Arkansas. Fayetteville, AR 72701, USA*

4. *Department of Physics. University of Belgrade. 11158 Belgrade, Serbia*

(Dated: February 18, 2014)

The geometry of two-dimensional crystalline membranes dictates their mechanical, electronic and chemical properties. The local geometry of a surface is determined from the two invariants of the metric and the curvature tensors. Here we discuss those invariants directly from atomic positions in terms of angles, areas, vertex and normal vectors from carbon atoms on the graphene lattice, for arbitrary elastic regimes and atomic conformations, and without recourse to an effective continuum model. The geometrical analysis of graphene membranes under mechanical load is complemented with a study of the local density of states (LDOS), discrete induced gauge potentials, velocity renormalization, and non-trivial electronic effects originating from the scalar deformation potential. The asymmetric LDOS is related to sublattice-specific deformation potential differences, giving rise to the pseudomagnetic field. The results here enable the study of geometrical, mechanical and electronic properties for arbitrarily-shaped graphene membranes in experimentally-relevant regimes without recourse to differential geometry and continuum elasticity.

PACS numbers: 73.22.Pr, 71.70.Di, 81.05.ue

Introduction.— Graphene [1, 2] belongs to a family of atom-thin elastic membranes [3] that conform to harder surfaces (e.g., [4]), develop ripples when freestanding [5–17], and can be deformed into arbitrary elastic regimes [18], leading to a remarkable electronic response [18–33]. In general, the local geometry of a two-dimensional (2D) surface is determined by four invariants of its metric (g) and curvature (k), that indicate how much it stretches and curves with respect to a reference non-deformed shape. Suitable choices are the determinant and the trace of g , the Gauss curvature $K \equiv \det(k)/\det(g)$, and the mean curvature $H \equiv \text{Tr}(k)/2\text{Tr}(g)$ [34–36].

In the existing literature, graphene's geometry is commonly studied in terms of a continuous displacement field $u_\alpha(\xi^1, \xi^2)$. Specifically, on thin-plate continuum elasticity the strain tensor is $u_{\alpha\beta} = (\partial_\alpha u_\beta + \partial_\beta u_\alpha + \partial_\alpha u_\beta \partial_\beta u_\alpha + \partial_\alpha z \partial_\beta z)/2$, with z an out-of-plane elongation [19–29, 33]. There, differential geometry and mechanics couple as:

$$g_{\alpha\beta} = \delta_{\alpha\beta} + 2u_{\alpha\beta}, \quad k_{\alpha\beta} = \hat{\mathbf{n}} \cdot \frac{\partial \mathbf{g}_\alpha}{\partial \xi^\beta}, \quad (1)$$

where $\mathbf{g}_\alpha(\xi^1, \xi^2)$ is a tangent vector field, $\delta_{\alpha\beta}$ is the reference (flat) metric and $\hat{\mathbf{n}} = \frac{\mathbf{g}_{\xi^1} \times \mathbf{g}_{\xi^2}}{|\mathbf{g}_{\xi^1} \times \mathbf{g}_{\xi^2}|}$ is the local normal. *Strain engineering clearly is a geometrical theory*, and differential geometry is the basis of this formalism as we know it [20–29, 33]. However, the geometrical description given by Eq. (1) has limitations. Continuum theory usually requires slow-varying, harmonic deformations, conditions that are violated in realistic situations [6, 39]. Peculiarities of how graphene ripples [6, 36–39], slides and adheres [6, 40] may be beyond first-order continuum elasticity.

This calls for a fundamental study of the geometry of atomistic membranes and their subsequent coupling

to electronic degrees of freedom, down to unavoidable atomic-scale fluctuations [13, 15]. Geometry is relevant in addressing spin diffusion in rippled graphene [41, 50], in understanding the chemical properties of conformal (non-planar) 2D crystals [42], and may even herald the strain engineering of 2D crystals with atomistic defects, an area completely unexplored so far.

In this Letter we develop a theoretical framework for strain engineering [10, 11, 43] based on discrete geometry, that applies to arbitrarily-shaped graphene without topological defects. Here, Wigner-Seitz unit cells are the underlying discrete geometrical objects and atomistic information is always preserved. The discrete formalism for geometry and the electronic response of Dirac fermions rests on interatomic distances without a mediating continuum. The framework here realized is *non-perturbative* on the geometry, and it can be used to indicate if the sublattice symmetry is preserved in the system at hand (this is assumed in the continuum theory [21]) and to show how the reciprocal space is renormalized by strain [33]. In what follows, we present the tools for geometrical analysis, study the local geometry of rippled graphene [13], and discuss the discrete geometry and the electronic properties of graphene under central load.

The discrete geometry.— The discrete metric is defined from the local lattice vectors \mathbf{a}_α [10, 11, 47] $g_{\alpha\beta} = \mathbf{a}_\alpha \cdot \mathbf{a}_\beta$ [Fig. 1(a-b)], and the discrete Gauss curvature (K_D) originates from the *angle defect* $\sum_{i=1}^6 \theta_i$ [44–46]:

$$K_D = (2\pi - \sum_{i=1}^6 \theta_i)/A_p. \quad (2)$$

Here θ_i ($i = 1, \dots, 6$) are angles between vertices shown in Fig. 1(a). The *Voronoi tessellation* [dark blue in Fig. 1(a)]

with an area A_p] generalizes the Wigner-Seitz unit cell on conformal 2D geometries. (The angle defect adds up to 2π on a flat surface, making $K_D = 0$, as expected.)

The discrete mean curvature H_D measures relative orientations of edges and normal vectors along a closed path:

$$H_D = \sum_{i=1}^6 \mathbf{e}_i \times (\boldsymbol{\nu}_{i,i+1} - \boldsymbol{\nu}_{i-1,i}) \cdot \hat{\mathbf{n}} / 4A_p. \quad (3)$$

Here, \mathbf{v}_i is the position of atom i on sublattice A , and $\mathbf{e}_i = \mathbf{v}_i - \mathbf{v}_p$ is the *edge* between points p and i (note that $\mathbf{a}_{1(2)} = \mathbf{e}_{1(2)}$). $\boldsymbol{\nu}_{i,i+1}$ is the normal to edges \mathbf{e}_i and \mathbf{e}_{i+1} (i is a cyclic index), and $\hat{\mathbf{n}} = \frac{\sum_{i=1}^6 \boldsymbol{\nu}_{i,i+1} A_i}{\sum_{i=1}^6 A_i}$ is the area-weighted normal with $A_i = |\mathbf{e}_i \times \mathbf{e}_{i+1}|/2$ [44]. For the purposes of discrete geometry, the metric and curvatures are formally decoupled objects.

The discrete metric and curvatures furnish geometry consistent with a crystalline structure, and lead to the faithful characterization of graphene's morphology beyond the effective-continuum paradigm, Eq. (1). This is advantageous when the atomic conformation is known from molecular dynamics (e.g., [13]) or experiment (e.g., [48]) because: (i) fitting of the atomic lattice to an effective continuum is not needed any more, (ii) the Chemistry of conformal graphene can be addressed from the discrete geometry [42] and, since atoms are always available, (iii) the discrete theory brings new insights and understanding into the physical theory (e.g., non-preservation of sublattice symmetry, the form of gauge fields [10], the creation of mass from strain [11, 29]). We emphasize that the discrete geometry is accurate regardless of elastic regime, hence it can be used to verify whether the conditions for continuum elasticity hold in the problem at hand.

Continuum geometry for small deformations.— The new framework does capture the known (continuum) geometry when the latter applies. This is illustrated in Fig. 1(c) for a profile $z(r) = A \exp[-r^2/\sigma^2]$ with $A=0.8$ Å and $\sigma=50$ Å [23]. The continuum geometrical invariants are: $\det(\tilde{g}) = 1 + 4r^2 z^2/\sigma^4$, $\text{Tr}(\tilde{g}) = 2 + 4r^2 z^2/\sigma^4$ (both are radial-symmetric), $\tilde{K} = \frac{z' z''}{r(1+z'^2)^2}$, and $\tilde{H} = \frac{z'}{2r\sqrt{1+z'^2}} + \frac{z''}{2(1+z'^2)^{3/2}}$. We next lay out a crystalline graphene lattice with discrete coordinates $(x_i, y_i, 0)$, and assign $z_i \equiv z(r_i)$ to each atom, with $r_i = \sqrt{x_i^2 + y_i^2}$. For easy comparison with the continuum metric, we renormalize g with respect to the flat discrete metric ($z_i = 0$) [$\det(g_{(0)}) = 3a_0^4/4$, and $\text{Tr}(g_{(0)})/2 = a_0^2$], and plot $1 - \sqrt{\det g}$ and $2 - \text{Tr}(g)$ to emphasize deviations from the reference metric. $\Delta\sqrt{\det(g)} \equiv \sqrt{\det(\tilde{g})} - \sqrt{\det(g)}$ and $\Delta\text{Tr}(g) \equiv \text{Tr}(\tilde{g}) - \text{Tr}(g)$ in Fig. 1(c) point to small discrepancies among the discrete (g) and continuum (\tilde{g}) [34, 35] metrics, originating already because \tilde{g} is built from tangent vector fields $\tilde{\mathbf{g}}_i$ as two points along a continuum geodesic collapse onto each other, and this limiting process does not take place on the atomic lattice [see Fig. 1(b)]. Those discrepancies aggravate under extreme morphologies for which the discrete geometry lacks

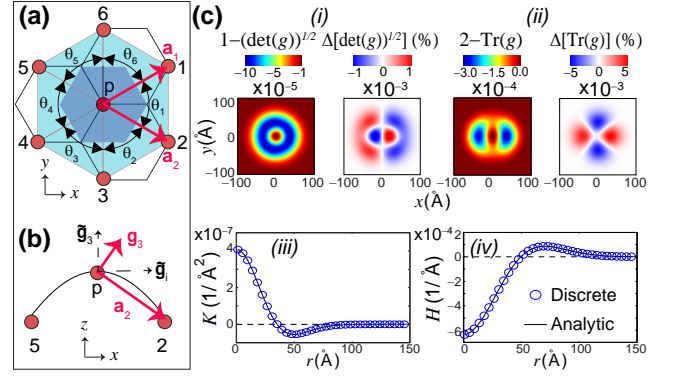


FIG. 1: (Color online) (a) Top view of polyhedra used to determine the four geometrical invariants from the metric and curvature. Circles represent atoms on the A-sublattice. Local lattice vectors are \mathbf{a}_1 and \mathbf{a}_2 ; θ_i are internal angles to edges \mathbf{e}_i and \mathbf{e}_{i+1} ; and the central shaded hexagon is the Voronoi cell. (b) Side view highlights the differences between continuum and discrete vector fields. (c) i: $\sqrt{\det(g)}$, ii: $\text{Tr}(g)$, iii: K and iv: H for a smooth gaussian bump where discrete and continuum results coincide. Percent differences $\sqrt{\det(g)} - \sqrt{\det(\tilde{g})}$ and $\text{Tr}(\tilde{g}) - \text{Tr}(g)$ are also shown.

smooth approximations in between atomic positions. On the other hand, $K_D = \tilde{K}$ and $H_D = \tilde{H}$ [Fig. 1(c)], highlighting the meaning of curvature from atoms [Eqs. (2-3)].

To make the discrete (g) and continuum (\tilde{g}) metrics correspond with one another, \tilde{g} must be corrected at atomic positions as follows: $g_{\alpha\beta} = b_\alpha^i b_\beta^j \tilde{g}_{ij} + b_\alpha^3 b_\beta^3$, where $\tilde{\mathbf{g}}_3 = \hat{\mathbf{n}} = \tilde{\mathbf{g}}_1 \times \tilde{\mathbf{g}}_2 / |\tilde{\mathbf{g}}_1 \times \tilde{\mathbf{g}}_2|$ and $b_\alpha^k = \mathbf{a}_\alpha \cdot \tilde{\mathbf{g}}_k$ ($\alpha, \beta = 1, 2$, and $i, j, k = 1, 2, 3$). The first term accounts for the anisotropy of the honeycomb lattice, while the second one is an *exponential map* that brings continuum tangent fields $\tilde{\mathbf{g}}_i$ back onto the atomistic surface [34, 36, 38].

Rippled graphene.— The importance of a sound geometrical framework is motivated by rippled graphene. We contrast ripples created by thermal fluctuations [13] with those created at low temperature due to edges. These two mechanisms lead to different types of geometries (hence different magnitudes of strain-derived gauges). In a system with periodic boundary conditions, thermal fluctuations create significant changes in interatomic distances (i.e., in the metric) [13] and—as the boundaries are fixed—such increases on interatomic distances reflect on out-of-plane deformations (i.e., rippling).

Now consider a square graphene sample with about three million atoms, and relieve strain at the edges at the low temperature of 1 Kelvin. The resulting membrane is shown in Fig. 2(a), where colors indicate varying heights across the sample [11]. Ripples in Ref. [13] originate from *increases* in the metric. On the other hand, the white margin in between the “rippled” (curved) sample and the (yellow) exterior frame highlights an apparent *contraction* of our finite sample when seen from above.

The details of this geometry are shown in Fig. 2(b).

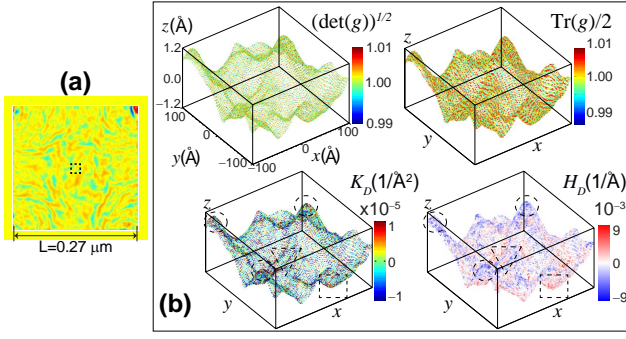


FIG. 2: (Color online) (a) Creation of ripples by cutting a square with side $L = 0.27 \mu\text{m}$ at 1 Kelvin: The membrane trades a planar configuration for a rippled one. (b) Geometrical invariants within the dashed square shown in (a).

We find that $\det(g)$ and $\text{Tr}(g)$ are unity almost everywhere (yet there are significant random fluctuations driving the scales): The metric tells us that the membrane does not contract and its area thus remains almost unchanged. We show in Fig. 2(b) the discrete curvatures, highlighting cusps by ovals, valleys by squares, and ridges by triangles. Cusps and valleys have the largest Gauss curvature K_D (deep red), while ridges have the smallest one (deep blue). As expected, the mean curvature H_D takes its largest (smallest) value at valleys (cusps) and alternates sign around ridges. The curvature –without metric increases– explains the white margins on Fig. 2(a).

The discrete geometry reflects the mechanism leading to ripple formation: This highlights the virtues of a geometry originating from atoms. In particular, an accurate determination of H_D is important since H_D leads to spin diffusion in rippled graphene [41, 50, 51]. Though much has been said about ripples, no geometrical study with the accuracy and insight provided here exists. The geometrical invariants in Fig. 2(b) are larger in magnitude than those in Fig. 1(c) –obtained by a smooth deformation from the reference ($z = 0$) initial configuration.

The starting point in the continuum theory is a flat metric $\delta_{\alpha\beta}$. There, a non-zero curvature directly leads to increases in interatomic distances [Eq. (1)], and a non-zero height is directly identified with a non-zero strain-derived gauge. A question then arises whether the sample under study actually obeys Eq. (1). The situation shown in Fig. 2 is a counterexample to the geometry inferred from Eq. (1) because the metric is almost constant even though the height profile z is clearly non-flat (for a pseudo-length-preserving distortion). Gauge fields for similar samples were reported in Ref. [11]. Rippled graphene is an excellent example that shows how crucial it is to know the exact geometry on a case-by-case basis, and Fig. 2 represents the accurate geometrical characterization of rippled graphene down to the atomic level.

Graphene under load.– Next we analyze a circular freestanding membrane [32] created by clamping the graphene sample in Fig. 2(a) outside a radius $R = 700$

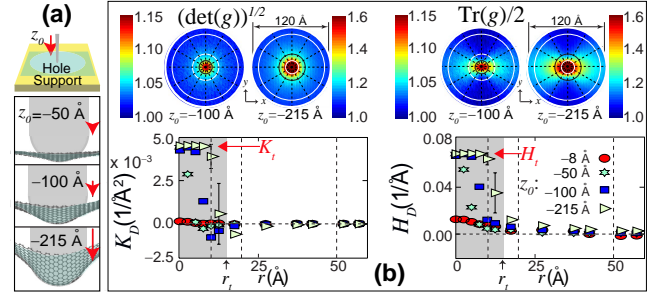


FIG. 3: (Color online) (a) Graphene under load by a semi-spherical tip of radius $r_t = 15 \text{\AA}$. (b) Geometrical invariants as the indentation proceeds. Under load, the metric increases unbounded, yet *curvatures can only saturate* to K_t and H_t as graphene conforms to the tip (see flat horizontal lines $K_D = K_t$ and $H_D = H_t$, for $0 \leq r \lesssim r_t$ at $z_0 = -100$ and -215\AA). Compare the trends with those in Fig. 1(c).

\AA from the geometrical center. We push the membrane *down* to a depth z_0 with a spherical tip of radius $r_t = 15 \text{\AA}$ [Fig. 3(a)]. The tip has constant curvatures $K_t \equiv 1/r_t^2 = 4.4 \times 10^{-3} \text{\AA}^{-2}$ and $H_t \equiv 1/r_t = 0.07 \text{\AA}^{-1}$.

Figure 3(b) tells us quantitatively how graphene gradually conforms to the tip pushing it down. g increases without bound (four upper plots in Fig. 3(b)) until an eventual mechanical breakdown [18]. $(\text{Tr}(g)/2)^{1/2}$ [from Fig. 3(b)] informs of large increases of interatomic distances, up to $\sim 26\%$ for loads where $z_0 = -215 \text{\AA}$ [10, 18], beyond the realm of first-order continuum elasticity [Eq. (1)]. The discrete metric g also uncovers an asymmetric elongation between armchair (vertical) and zigzag (horizontal) directions which the continuum metric \tilde{g} does not capture unless corrected as indicated above.

On the other hand, graphene cannot acquire a curvature higher than that of the tip, so K_D and H_D must be bounded. This is precisely the content of the two lower plots in Fig. 3(b): For small loads ($z_0 = -8 \text{\AA}$; ellipses) the curvatures are almost zero as expected. Curvatures increase (star, rectangle and triangle) as the magnitude of z_0 increases ($z_0 = -50, -100$, and -215\AA , respectively). The important observation is that curvatures saturate ($K_D \rightarrow K_t$ and $H_D \rightarrow H_t$) for distances r within r_t (shaded area), confirming the qualitative conformal shape depicted on Fig. 3(a). K_D and H_D have analogous trends in Figs. 1 and 3 [H_D is a signed quantity, having opposite signs for a bulge (Fig. 1) and a sag (Fig. 3)]. Yet, it remains a challenge to accurately describe the geometry shown in Fig. 3 within the continuum formalism using Eq. (1). This is so, because for high load the metric and curvature appear decoupled, while in the continuum approach they are inexorably inter-related.

Microscopic mass term and gauge fields.– Next, we analyze electronic properties of graphene under load by the tip. We first re-express the microscopic pseudo-magnetic field from the curl of the (pseudomagnetic) vector potential. This is accomplished with a second-order difference

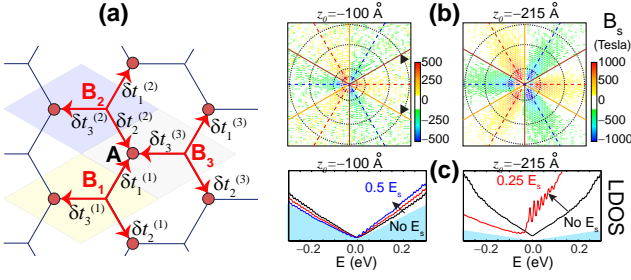


FIG. 4: (Color online) (a) The finite-difference curl leading to the pseudomagnetic field B_s [Eq. 4] is obtained from hoppings among an atom on the A-sublattice, and three neighboring atoms on B-sublattices. (b) B_s for $z_0 = -100$ and -215 Å loads. (c) LDOS with screened values of the deformation potential E_s at $r = 0$, for $z_0 = -100$ and -215 Å.

relation among potential energies for an atom on the A-sublattice at the K -point [Fig. 4(a)] [2, 29, 47, 51]:

$$-\mu_B B_s = \frac{\sqrt{3}\hbar^2}{m_e a_0^2 t} ((\delta t_3^{(3)} - \delta t_1^{(3)}) - (\delta t_3^{(2)} - \delta t_1^{(2)})) + (\delta t_3^{(3)} - \delta t_2^{(3)}) - (\delta t_3^{(1)} - \delta t_2^{(1)})). \quad (4)$$

Here, μ_B is the Bohr magneton ($\simeq 5.8 \times 10^{-5}$ eV/Tesla), $\delta t_j^{(n)}$ is the standard change in hopping upon strain at unit cell $n = 1, 2, 3$ [10, 19, 21, 22], and $\frac{\sqrt{3}\hbar^2}{m_e a_0^2 t} \simeq 2.5$ [47]. The pseudomagnetic field B_s changes sign at the B-sublattice and/or at the K' point [2, 51]. E_s is the average deformation potential at a given unit cell (see Refs. [10] and [47]) arising from the rearrangement of the electron cloud upon strain [19]. B_s is shown on Fig. 4(b) for $z_0 = -100$ and $z_0 = -215$ Å within a 75 Å radius from the tip.

Local density of states.— The shaded area plots on Fig. 4(c) and Fig. 5(a-b) are reference LDOS obtained from a flat configuration with no strain. The metric and curvature in Fig. 3(b) take extreme values at $r = 0$, and the LDOS in Fig. 4(c) increase in slope as the Fermi velocity v_F becomes more and more renormalized [23, 25] as $LDOS \propto 1/v_F^2$ [2]. Remarkably, in the scenario given by Fig. 3(b), the metric increase enhances the velocity renormalization while, at the same time, the curvature remains the same. This is so because the observed Fermi velocity renormalization is related to g : Indeed, it is caused by changes in interatomic distances [19, 22].

When a screened E_s is applied, v_F renormalization becomes electron-hole asymmetric [2, 48], and a sequence of equally-spaced peaks arise even without explicit inclusion of spin (we do not have a quartet-splitting mechanism [32]). Thus, our results suggest an alternative explanation for the identically-spaced LDOS features observed in a similar experimental setup [32] (in particular, refer to Fig. 4(c) with $z_0 = -215$ Å, where E_s is larger). We emphasize that there is no central LDOS peak (‘zeroth Landau level’) for circular membranes under load.

The dashed LDOS curves in Fig. 5 were plotted with

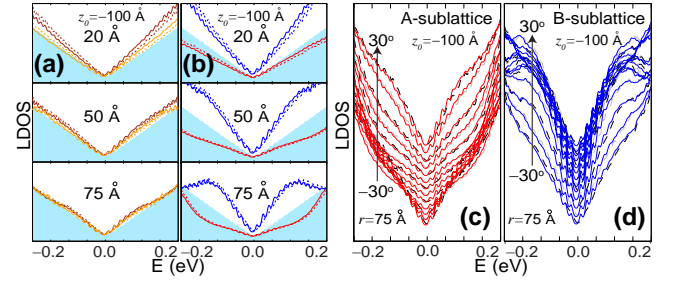


FIG. 5: (Color online) A-sublattice LDOS along the (a) -30° and (b) $+30^\circ$ axes ($z_0 = -100$ Å). Angular sweeps at $r = 75$ Å on the (c) A- and (d) B-sublattices ($z_0 = -100$ Å): Due to time-reversal symmetry, a sign change in B_s in (b) has the same effect as a sublattice exchange (c-d).

$E_s = 0$, while the asymmetric LDOS profiles –displaying equally-spaced peaks– were obtained with a (screened) $0.25E_s$ deformation potential. On Figs. 5(a-b) we explore the LDOS in space and *exclusively* on the A-sublattice, generated from a $z_0 = -100$ Å load. Figure 5(a) shows the LDOS along the -30° (orange/light) and $+30^\circ$ (brown/dark) radial axes on the polar grid in display on Figs. 3(c) and 4(b). Due to threefold-symmetry, the LDOS is identical upon 120° rotations. $B_s \sim 0$ in Fig. 5(a) as it alternates sign at those axes. Hence, the only observable effect is a LDOS renormalization due to the metric [23] ($r = 20$ Å plot). The renormalization gradually decreases with increasing r until the LDOS overlaps with the reference one (see $r = 75$ Å plot), consistent with a metric approaching the flat one [Fig. 3(b)]. On the other hand, under a non-zero B_s the LDOS on the A-sublattice either becomes enhanced (blue curves; $B_s < 0$; 60° axis) or suppressed (red; $B_s > 0$; 0° axis) with respect to the reference LDOS [Fig. 5(b)]. Figure 4(a) complements previous reports [54].

Due to time-reversal symmetry, the A- and B-sublattices are subjected to B_s with opposite signs and the behavior on Fig. 5(b) should be reproducible by exploring the LDOS under the same B_s , but now at the B-sublattice (exchanging K to K' amounts to a sublattice exchange [48]). This is verified on Fig. 5(c-d) by the sublattice resolved angular sweep across a $B_s > 0$ feature. A sublattice asymmetric LDOS [Fig. 5(c-d)] is consistent with a sublattice-dependent potential, Eq. 4, [11, 29] through Coulomb’s law.

Conclusion.— We presented a discrete approach to study graphene’s geometry and its electron properties without relying on continuum approximations and beyond thin-plate continuum mechanics. We used the method to study the experimentally relevant situations of rippled graphene and graphene under large mechanical load. Our theory fully respects the discrete geometry of arbitrarily-shaped graphene, thus opening a completely unexplored and promising route for strain-engineering beyond the restrictions of small and slowly-varying deformations inherent to continuum theories. We thank M.A.H. Voz-

mediano, D. Kennefick, and M. Mehboudi. We carried calculations at TACC (*Stampede*; TG-PHY090002) and Arkansas. M. V. acknowledges the Serbian Ministry of Science, Project 171027.

Supplementary Information:

Definition of metrics.- Given two in-plane vector fields \mathbf{g}_1 and \mathbf{g}_2 , metrics $g_{\alpha\beta} \equiv \mathbf{g}_\alpha \cdot \mathbf{g}_\beta$ are symmetric ($g_{\alpha\beta} = g_{\beta\alpha}$) and positive-definite ($g_{\alpha\alpha} > 0$) ($\alpha, \beta = 1, 2$).

The continuum geometry.- Differential geometry and first-order continuum mechanics couple as:

$$g_{\alpha\beta} = \delta_{\alpha\beta} + 2u_{\alpha\beta}; \quad k_{\alpha\beta} = \hat{\mathbf{n}} \cdot \mathbf{g}_{\alpha;\beta} \equiv \hat{\mathbf{n}} \cdot \frac{\partial \mathbf{g}_\alpha}{\partial \xi^\beta} + \Gamma_{\alpha\beta}^3. \quad (5)$$

As it turns out, the connection $\Gamma_{\alpha\beta}^3$ is identically zero, leading to Equation 1 on the main manuscript.

The realm of discrete differential geometry.- The aims and scope of discrete differential geometry (DDG) are given here by adapting work of Bobenko and Suris [45] to graphene's context.

The goal of DDG is to develop mathematically sound relations between differential and discrete geometry [44, 45]. Classical, *Riemannian* differential geometry studies the properties of smooth, continuum objects, and *discrete* geometry studies geometrical shapes made of polyhedra. DDG, in turn, seeks for discrete equivalents of notions and methods of continuous Riemannian geometry. Given that graphene's lattice is made of polyhedra, it represents a physically-relevant system for DDG.

To realize theories consistent with DDG one first determines a proper discrete surface, and develops theory *from that discrete surface*. In the absence of an actual atomic lattice, one can suggest many different discretizations of surfaces having the same continuum limit. For graphene, on the other hand, the honeycomb lattice *is* the discrete lattice, and no more fundamental choice exists without involving approximations.

This represents a central difference between an all-discrete theory and discrete approximations of continuum models. In the latter, discretization of surfaces and differential equations is carried out on an arbitrary mesh. In the context of strain engineering in graphene, this process starts the moment the theory of an effective continuum media [19, 21, 22] is mapped onto arbitrary meshes for numerical analysis. In applying DDG to graphene, on the other hand, the mesh is given by the deformed honeycomb lattice, and we never take the continuum limit of the pseudospin Hamiltonian when considering the electronic behavior either [10, 11]. The results of DDG are therefore non-perturbative on graphene's atomistic morphology.

Discrete geometry for substantial distortions.- On page 2 of the main manuscript we demonstrate that the discrete and continuum geometries agree in the limit of small deformations; this is, when the distortion is small when

compared to interatomic distances. For large deformations, the continuum hypothesis breaks down as continuum tangent fields cannot be generated to arbitrary precision from atomic locations.

To show the breakdown of the continuum geometrical description, we display in Fig. 1 the geometry for the function $z(x_i, y_i) = A(\exp[-\frac{(x_i-x_0)^2+y_i^2}{\sigma^2}] - \exp[-\frac{(x_i+x_0)^2+y_i^2}{\sigma^2}])$, with $A = 25 \text{ \AA}$, $\sigma = 30 \text{ \AA}$, and $x_0 = 25 \text{ \AA}$. Here, the continuum geometrical invariants display large discrepancies to the discrete geometry; this is particularly the case for the trace of the metric.

As a consequence of such discrepancies, the continuum idealization of the atomic membrane will have an inaccurate distribution of in-plane local forces/stress, and will be incompatible with the actual lattice structure. A subtler deficiency, tangent vectors $\tilde{\mathbf{g}}_i$ ($i = 1, 2$) may *lie outside* of the polygonal surface [Fig. 1(b) on the main text], compromising mechanical equilibrium. An exponential map bringing the continuum vector field $\tilde{\mathbf{g}}_i$ back onto the atomistic surface becomes necessary, and the continuum metric \tilde{g} must be corrected at atomic positions to properly conform to g :

$$g_{\alpha\beta} = b_\alpha^i b_\beta^j \tilde{g}_{ij} + b_\alpha^3 b_\beta^3, \quad (6)$$

as indicated on Page 2 of the main manuscript. The first term on Eq. (6) accounts for the anisotropy of the atomic distortion and the second one is the exponential map. In looking at Figure 1, it is important to note that curvatures are much more better behaved in between descriptions, highlighting once again the deep significance of curvature from atoms, Eqns. 2 and 3 on the main text.

The mean deformation potential E_s .- This empirical expression was introduced before (Eqn. (18) in Ref. [10]), where we proposed it to be linearly proportional to the average increases in bond lengths. E_s is radially-symmetric, and it has the radial shape illustrated in Fig. 7 for loads $z_0 = -100 \text{ \AA}$, and $z_0 = -215 \text{ \AA}$.

Derivation of the pseudo-magnetic field.- Changes in distances between atoms upon strain modify the local electrostatic potential [11]. Proper consideration of those changes on the local potential cannot be given by consideration of nearest neighbors alone, and a second-order difference equation is needed. Here we derive microscopic expressions for the pseudo-magnetic field, when the zigzag direction is parallel to the y-axis [10]. Results for the other common choice (i.e., zigzag direction parallel to x-axis [21, 22]) can be obtained along similar lines.

The program of action is as follows: We wish to express the magnitude of the finite-difference pseudo-magnetic field B_s as a function of local changes on δt in between sublattices from terms leading to the vector potential. B_s will display a straightforward and physically intuitive form in terms of energy variations δt among neighboring atoms belonging to complementary sublattices. These variations are similar in origin to the ones we reported

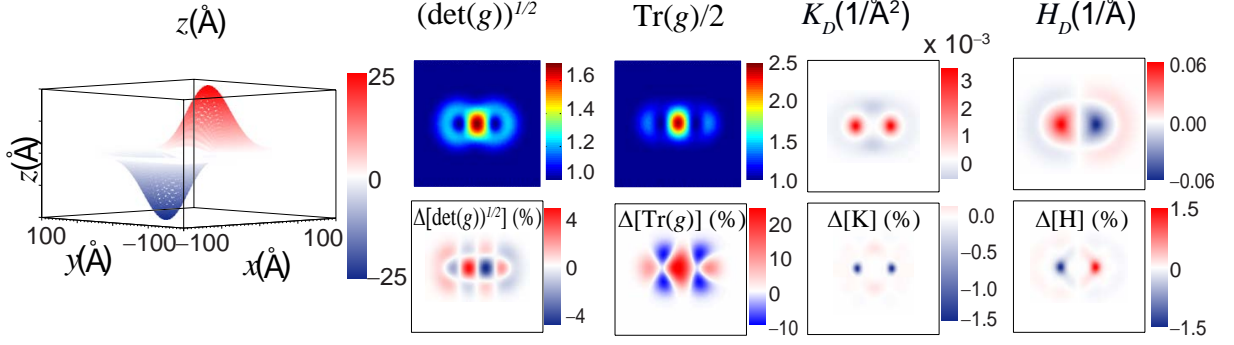


FIG. 6: (Color online) Discrepancies among the continuum and discrete geometries for a large deformation.

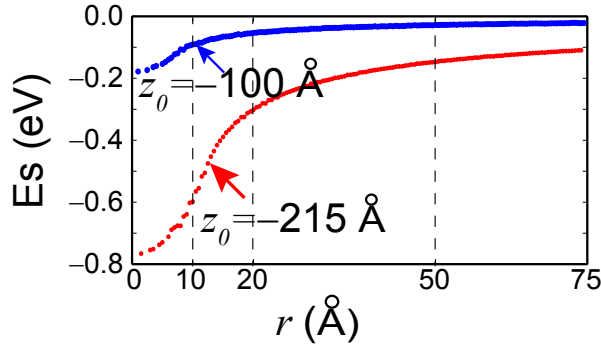


FIG. 7: (Color online) Radial profile of the deformation potential E_s .

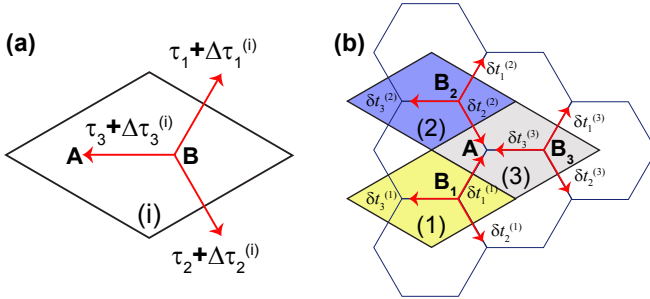


FIG. 8: (Color online) Schematics of local deformations required in determining the magnitude of the pseudo-magnetic field by finite differences.

before [11], but with the symmetry of a Zeeman term [29] built in.

We set the zigzag direction to be parallel to the y-axis, and start with the standard expression leading to the vector potential:

$$\sum_{j=1}^3 \delta t_j e^{i\mathbf{K} \cdot \boldsymbol{\tau}_j}, \quad (7)$$

where $\boldsymbol{\tau}_1 = (1/2, \sqrt{3}/2)a_0/\sqrt{3}$, $\boldsymbol{\tau}_2 = (1/2, -\sqrt{3}/2)a_0/\sqrt{3}$, and $\boldsymbol{\tau}_3 = (-1, 0)a_0/\sqrt{3}$. $\delta t_j = -|\beta|t\boldsymbol{\tau}_j \cdot \Delta\boldsymbol{\tau}_j/a_0^2$, see [10, 22] for details. We choose $\mathbf{K} = (0, 1)_{\frac{4\pi}{3a_0}}$ as well. Then:

$$\sum_{j=1}^3 \delta t_j^{(n)} e^{i\mathbf{K} \cdot \boldsymbol{\tau}_j} = \quad (8)$$

$$-\frac{\sqrt{3}}{2} \left[\frac{2\delta t_3^{(n)} - \delta t_1^{(n)} - \delta t_2^{(n)}}{\sqrt{3}} + i(\delta t_1^{(n)} - \delta t_2^{(n)}) \right].$$

The upper index (n) enters in Eq. (8) because the discrete curl (a term arising from differences of δt in between sublattices) requires obtaining differences of $\sum_{j=1}^3 \delta t_j^{(n)} e^{i\mathbf{K} \cdot \boldsymbol{\tau}_j}$ on three adjacent unit cells Fig. 8; $n = 1, 2, 3$. Consistent with the choice of zigzag direction, the x and y components of the vector potential dictate the choice of components in Eq. (8) [10]. To simplify the algebra, we introduce:

$$f_x(A) \equiv \delta t_2^{(2)} - \delta t_1^{(1)}, \quad f_y(A) \equiv \frac{2\delta t_3^{(3)} - \delta t_1^{(1)} - \delta t_2^{(2)}}{\sqrt{3}},$$

$$f_x(B_1) \equiv \delta t_2^{(1)} - \delta t_1^{(1)}, \quad f_y(B_1) \equiv \frac{2\delta t_3^{(1)} - \delta t_1^{(1)} - \delta t_2^{(1)}}{\sqrt{3}},$$

$$f_x(B_2) \equiv \delta t_2^{(2)} - \delta t_1^{(2)}, \quad f_y(B_2) \equiv \frac{2\delta t_3^{(2)} - \delta t_1^{(2)} - \delta t_2^{(2)}}{\sqrt{3}},$$

$$f_x(B_3) \equiv \delta t_2^{(3)} - \delta t_1^{(3)}, \quad f_y(B_3) \equiv \frac{2\delta t_3^{(3)} - \delta t_1^{(3)} - \delta t_2^{(3)}}{\sqrt{3}}. \quad (9)$$

We use Eq. (9) to establish the discrete local curl in terms of differences of function $\mathbf{f} = (f_x, f_y)$ at neighboring positions corresponding to complementary sublattices:

$$\Delta \times \mathbf{f} \equiv (\Delta_x f_y - \Delta_y f_x) \hat{\mathbf{n}}. \quad (10)$$

Then, finite-differences become:

$$\Delta_x f_y = \frac{f_y(A) - f_y(B_3)}{(\boldsymbol{\tau}_3 + \Delta\boldsymbol{\tau}_3) \cdot \hat{\mathbf{i}}} + \frac{f_y(A) - f_y(B_2)}{(\boldsymbol{\tau}_2 + \Delta\boldsymbol{\tau}_2) \cdot \hat{\mathbf{i}}} + \frac{f_y(A) - f_y(B_1)}{(\boldsymbol{\tau}_1 + \Delta\boldsymbol{\tau}_1) \cdot \hat{\mathbf{i}}} \quad (11)$$

and:

$$\Delta_y f_x = \frac{f_x(A) - f_x(B_2)}{(\boldsymbol{\tau}_2 + \Delta\boldsymbol{\tau}_2) \cdot \hat{\mathbf{j}}} + \frac{f_x(A) - f_x(B_1)}{(\boldsymbol{\tau}_1 + \Delta\boldsymbol{\tau}_1) \cdot \hat{\mathbf{j}}}. \quad (12)$$

$\hat{\mathbf{i}}$ and $\hat{\mathbf{j}}$ represent local in-plane vector fields:

$$\hat{\mathbf{i}} \equiv \frac{\mathbf{a}_1 + \mathbf{a}_2}{|\mathbf{a}_1 + \mathbf{a}_2|}; \quad \hat{\mathbf{j}} \equiv \frac{\mathbf{a}_1 - \mathbf{a}_2}{|\mathbf{a}_1 - \mathbf{a}_2|}, \quad (13)$$

with $\mathbf{a}_1 = \boldsymbol{\tau}_1 + \Delta\boldsymbol{\tau}_1^{(3)} - (\boldsymbol{\tau}_3 + \Delta\boldsymbol{\tau}_3^{(3)})$ and $\mathbf{a}_2 = \boldsymbol{\tau}_2 + \Delta\boldsymbol{\tau}_2^{(3)} - (\boldsymbol{\tau}_3 + \Delta\boldsymbol{\tau}_3^{(3)})$ the local lattice displacements for a central atom on the A -sublattice, and $\hat{\mathbf{n}}$ was defined in Eq. 2 in the main text. Using Eq. (9), we get for Eqs. (11) and (12):

$$\Delta_x f_y = \frac{(\delta t_1^{(3)} + \delta t_2^{(3)}) - (\delta t_1^{(1)} + \delta t_2^{(2)})}{(\boldsymbol{\tau}_3 + \Delta\boldsymbol{\tau}_3^{(3)}) \cdot \hat{\mathbf{i}}} + \frac{2\delta t_3^{(3)} - \delta t_1^{(1)} - (2\delta t_3^{(2)} - \delta_1^{(2)})}{(\boldsymbol{\tau}_2 + \Delta\boldsymbol{\tau}_2^{(2)}) \cdot \hat{\mathbf{i}}} + \frac{2\delta t_3^{(3)} - \delta t_2^{(2)} - (2\delta t_3^{(1)} - \delta_2^{(1)})}{(\boldsymbol{\tau}_1 + \Delta\boldsymbol{\tau}_1^{(1)}) \cdot \hat{\mathbf{i}}}, \quad (14)$$

and:

$$\Delta_y f_x = \frac{\delta t_1^{(2)} - \delta t_1^{(1)}}{(\boldsymbol{\tau}_2 + \Delta\boldsymbol{\tau}_2^{(2)}) \cdot \hat{\mathbf{j}}} + \frac{\delta t_2^{(2)} - \delta t_2^{(1)}}{(\boldsymbol{\tau}_1 + \Delta\boldsymbol{\tau}_1^{(1)}) \cdot \hat{\mathbf{j}}}. \quad (15)$$

Next, we require hermiticity of a vector potential (these conditions are not needed for a scalar potential term, which is Hermitian by construction). The conditions are (see [21] and [10, 11] for extended discussion):

$$\boldsymbol{\tau}_1 + \Delta\boldsymbol{\tau}_1^{(1)} \rightarrow \boldsymbol{\tau}_1 + \Delta\boldsymbol{\tau}_1^{(3)}, \text{ and } \boldsymbol{\tau}_2 + \Delta\boldsymbol{\tau}_2^{(2)} \rightarrow \boldsymbol{\tau}_2 + \Delta\boldsymbol{\tau}_2^{(3)}. \quad (16)$$

An immediate consequence from Eq. (16) is that $\delta t_1^{(1)} \rightarrow \delta t_1^{(3)}$ and $\delta t_2^{(2)} \rightarrow \delta t_2^{(3)}$ as well. Therefore, Eqs. (11) and (12) take the final form:

$$\Delta_x f_y = \frac{2\delta t_3^{(3)} - \delta t_1^{(4)} - (2\delta t_3^{(2)} - \delta_1^{(2)})}{(\boldsymbol{\tau}_2 + \Delta\boldsymbol{\tau}_2^{(3)}) \cdot \hat{\mathbf{i}}} + \frac{2\delta t_3^{(3)} - \delta t_2^{(3)} - (2\delta t_3^{(1)} - \delta_2^{(1)})}{(\boldsymbol{\tau}_1 + \Delta\boldsymbol{\tau}_1^{(3)}) \cdot \hat{\mathbf{i}}}, \quad (17)$$

and

$$\Delta_y f_x = \frac{\delta t_1^{(2)} - \delta t_1^{(3)}}{(\boldsymbol{\tau}_2 + \Delta\boldsymbol{\tau}_2^{(3)}) \cdot \hat{\mathbf{j}}} + \frac{\delta t_2^{(3)} - \delta t_2^{(1)}}{(\boldsymbol{\tau}_1 + \Delta\boldsymbol{\tau}_1^{(3)}) \cdot \hat{\mathbf{j}}}. \quad (18)$$

Equation (10) as derived here supersedes our previous expression for the curl leading to the pseudo-magnetic field [10]. Equation (10) together with Eqs. (17) and (18) were employed in plotting Fig. 4(b) in the main text.

The following approximation helps the reader in better grasping the origin of the curl from differences of changes of on-site potentials upon strain (i.e., a ‘second-order’ differences equation). If we set $\frac{1}{(\boldsymbol{\tau}_j + \Delta\boldsymbol{\tau}_j^{(n)}) \cdot \hat{\mathbf{i}}} \simeq \frac{1}{\boldsymbol{\tau}_j \cdot \hat{\mathbf{i}}}$ (and

a similar approximation for the term involving projection onto $\hat{\mathbf{j}}$), then the vector projections on the denominator can be carried out easily, and the finite-differences curl takes the following rather intuitive form:

$$|\Delta \times \mathbf{f}| = \Delta_x f_y - \Delta_y f_x = \frac{4}{a_0} [(\delta t_3^{(3)} - \delta t_1^{(3)}) + (\delta t_3^{(3)} - \delta t_2^{(3)}) + (\delta t_1^{(2)} - \delta t_3^{(2)}) + (\delta t_2^{(1)} - \delta t_3^{(1)})]. \quad (19)$$

This way:

$$\mathbf{B}_s = -2\sqrt{3} \frac{\phi_0}{\pi a_0^2 t} \times ((\delta t_3^{(3)} - \delta t_1^{(3)}) + (\delta t_3^{(3)} - \delta t_2^{(3)}) + (\delta t_1^{(2)} - \delta t_3^{(2)}) + (\delta t_2^{(1)} - \delta t_3^{(1)})) \hat{\mathbf{n}}, \quad (20)$$

($\hat{\mathbf{n}} = \hat{\mathbf{z}}$ is the local normal; all constants were defined before [10]; $a_0 = 1.391$ at 1 Kelvin), and the curl finally becomes Eq. 4 in the main text:

$$-\mu_B B_s = 2\sqrt{3}g \frac{e\hbar}{4m_e \pi a_0^2 t} \times ((\delta t_3^{(3)} - \delta t_1^{(3)}) + (\delta t_3^{(3)} - \delta t_2^{(3)}) + (\delta t_1^{(2)} - \delta t_3^{(2)}) + (\delta t_2^{(1)} - \delta t_3^{(1)})). \quad (21)$$

g is the Landé factor, which we set equal to 2. The Landé factor g , along with m_e –the electron mass– are external parameters of the theory. The prefactor is dimensionless:

$$2\sqrt{3}g \frac{e\hbar}{4m_e \pi a_0^2 t} = 2\sqrt{3} \frac{g\hbar^2}{4m_e a_0^2 t} \simeq 2.5. \quad (22)$$

B_s changes sign upon sublattice exchange or K -point exchange. Eq. (15) is related to the staggered DOS observed experimentally, giving additional insight as to how the discrete geometry of graphene couples to its electronic properties.

Consequences for spin-orbit coupling estimates.– The concepts presented in the main text can be used for an accurate determination of the spin-orbit coupling $\Delta(\mathbf{r}_i)$ induced by curvature. In the absence of strain $\Delta(\mathbf{r}_i) \propto H_D(\mathbf{r}_i)$ [41, 50]. An estimate from H_D in Fig. 2(c) in the main text yields $-0.2 \text{ meV} \lesssim \Delta \lesssim 0.2 \text{ meV}$ [41]. We note that $\Delta(\mathbf{r}_i)$ changes sign with H_D . The proportionality between H_D and Δ depends on hopping invariants that decay exponentially with distance: A more general expression for $\Delta(\mathbf{r}_i)$ must depend on the metric g as well.

H_D increases by an order of magnitude and changes sign in between Figs. 2(c) and 3(c) in the main text, making $|\Delta| \lesssim 2 \text{ meV}$ under central load –even when ignoring effects due to g . As we employed a smearing parameter $\sigma = 5 \text{ meV}$ in plotting LDOS curves, we were unable to resolve spin-orbit coupling, which was hence ignored in the main text.

-
- [1] P. Wallace, Phys. Rev. **71**, 622 (1947); A. K. Geim and K. S. Novoselov, Nature Materials **6**, 183 (2007); Y. Zhang, Y.-W. Tan, H. L. Stormer and P. Kim, Nature **438**, 201 (2005); C. Berger, Z. Song, T. Li, X. Li, A. Y. Ogbazghi, R. Feng, Z. Dai, A. N. Marchenkov, E. H. Conrad, P. N. First, and W. A. de Heer, J. Phys. Chem. B **108**, 19912 (2004).
- [2] A. H. Castro-Neto, F. Guinea, N. M. R. Peres, K. S. Novoselov and A. K. Geim, Rev. Mod. Phys. **81**, 109 (2009).
- [3] K. S. Novoselov, D. Jiang, F. Schedin, T. J. Booth, V. V. Khotkevich, S. V. Morozov and A. K. Geim, Proc. Natl. Acad. Sci. (USA) **102**, 10451 (2005); A. K. Geim and I. V. Grigorieva, Nature **499**, 419 (2013); S. Z. Butler, S. M. Hollen, L. Cao, Y. Cui, J. A. Gupta, H. R. Gutiérrez, T. F. Heinz, S. S. Hong, J. Huang, A. F. Ismach, E. Johnston-Halperin, M. Kuno, V. V. Plashnitsa, R. D. Robinson, R. S. Ruoff, S. Salahuddin, J. Shan, L. Shi, M. G. Spencer, M. Terrones, W. Windl and J. E. Goldberger ACS Nano **7**, 2898 (2013); H. L. Zhuang, A. K. Singh and R. G. Hennig, Phys. Rev. B **87**, 165415 (2013).
- [4] S. Morozov, K. S. Novoselov, M. I. Katsnelson, F. Schedin, L. A. Ponomarenko, D. Jiang and A. K. Geim, Phys. Rev. Lett. **97**, 016801 (2006); M. I. Katsnelson and A. K. Geim, Phil. Trans. R. Soc. A **366**, 195 (2008); N. Mohanty, M. Fahrenholtz, A. Nagaraja, D. Boyle and V. Berry, Nano Lett. **11**, 1270 (2011); M. Yamamoto, O. Pierre-Louis, J. Huang, M. S. Fuhrer, T. L. Einstein, and W. G. Cullen, Phys. Rev. X **2**, 041018 (2012).
- [5] J. C. Meyer, A. K. Geim, M. I. Katsnelson, K. S. Novoselov, T. J. Booth and S. Roth, Nature **446**, 60 (2007); M. Gass, U. Bangert, A. L. Bleloch, P. Wang, R. R. Nair and A. K. Geim, Nature Nanotechnology **3**, 676 (2008).
- [6] L. Tapasztó, T. Dumitrica, S. J. Kim, P. Nemes-Incze, C. Hwang and L. P. Biro, Nature Phys. **8**, 739 (2012).
- [7] V. Shenoy, C. D. Reddy, A. Ramasubramaniam and Y. W. Zhang, Phys. Rev. Lett. **101**, 245501 (2008).
- [8] B. Huang, M. Liu, N. Su, J. Wu, W. Duan, B.-L. Gu and F. Liu, Phys. Rev. Lett. **102**, 166404 (2009).
- [9] H. Wang and Moneesh Upmanyu, Phys. Rev. B **86**, 205411 (2012).
- [10] J. V. Sloan, A. A. Pacheco Sanjuan, Z. Wang, C. Horvath and S. Barraza-Lopez, Phys. Rev. B **87**, 155436 (2013).
- [11] S. Barraza-Lopez, A. A. Pacheco Sanjuan, Z. Wang and Mihajlo Vanević, Solid State Comm. **166**, 70 (2013).
- [12] H. Vandeplas, M. Piñeirua, F. Brau, B. Roman, J. Bico, C. Gay, W. Bao, C. N. Lau, P. M. Reis and Pascal Damman, Phys. Rev. Lett. **106**, 224301 (2011).
- [13] A. Fasolino, J. H. Los and M. I. Katsnelson, Nature Materials **6**, 858 (2007).
- [14] K. Zakharchenko, R. Roldán, A. Fasolino and M. I. Katsnelson, Phys. Rev. B **82**, 125435 (2010).
- [15] K. Zakharchenko, M. I. Katsnelson and A. Fasolino, Phys. Rev. Lett. **102**, 046808 (2009).
- [16] M. Gibertini, A. Tomadin and M. Polini, Phys. Rev. B **81**, 125437 (2010).
- [17] P. San-Jose, J. González and F. Guinea, Phys. Rev. Lett. **106**, 045502 (2011).
- [18] C. Lee, X. Wei, J. W. Kysar and J. Hone, Science **321**, 385 (2008); G. H. Lee, R. C. Cooper, S. J. An, S. Lee, A. van der Zande, N. Petrone, A. G. Hammerberg, C. Lee, B. Crawford, W. Oliver, J. W. Kysar and J. Hone, Science **340**, 1073 (2013).
- [19] H. Suzuura and T. Ando, Phys. Rev. B **65**, 235412 (2002).
- [20] V. M. Pereira and A. H. Castro Neto, Phys. Rev. Lett. **103**, 046801 (2009).
- [21] F. Guinea, and M. I. Katsnelson and A. K. Geim, Nature Physics **6**, 30 (2010).
- [22] M. A. H. Vozmediano, and M. I. Katsnelson, and F. Guinea, Phys. Rep. **496**, 109 (2010).
- [23] F. de Juan, A. Cortijo and M. A. H. Vozmediano, Phys. Rev. B **76**, 165409 (2007).
- [24] F. de Juan, A. Cortijo, M. A. H. Vozmediano and A. Cano, Nature Phys. **7**, 810 (2011).
- [25] F. de Juan, M. Sturla and M. A. H. Vozmediano, Phys. Rev. Lett. **108**, 227205 (2012).
- [26] M. Neek-Amal, L. Covaci, and F. M. Peeters, Phys. Rev. B **86**, 041405(R) (2012).
- [27] D. M. M. R. Masir, D. Moldovan and F. M. Peeters, Solid State Comm. **175-176**, 76 (2013).
- [28] R. Kerner, G. G. Naumis and W. A. Gómez-Arias, Physica B **407**, 2002 (2012).
- [29] J. Mañes, F. de Juan, M. Sturla and M. A. H. Vozmediano, Phys. Rev. B **88**, 155405 (2013).
- [30] N. Levy, S. A. Burke, K. L. Meaker, M. Panlasigui, A. Zettl, F. Guinea, A. H. Castro-Neto and M. F. Crommie, Science **329**, 544 (2010).
- [31] P. Xu, Y. Yang, S. D. Barber, M. L. Ackerman, J. K. Schöelz, D. Qi, I. A. Kornev, L. Dong, L. Bellaiche, S. Barraza-Lopez and P. M. Thibado, Phys. Rev. B **85**, 121406(R) (2012); R. Zan, C. Muryn, U. Bangert, P. Mattocks, P. Wincott, D. Vaughan, X. Li, L. Colombo, R. S. Ruoff, B. Hamilton and K. S. Novoselov, Nanoscale **4**, 3065 (2012); F. R. Eder, J. Kotakoski, K. Holzweber, C. Mangler, V. Skakalova and J. C. Meyer, Nano Lett. **13**, 1934 (2013).
- [32] N. N. Klimov, S. Jung, S. Zhu, T. Li, C. A. Wright, S. D. Solares, D. B. Newell, N. B. Zhitenev and J. A. Stroscio, Science **336**, 1557 (2012).
- [33] A. L. Kitt, V. M. Pereira, A. K. Swan and B. B. Goldberg, Phys. Rev. B **87**, 159909(E) (2013); F. de Juan, J. L. Mañes and M. A. H. Vozmediano, Phys. Rev. B **87**, 165131 (2013); M. Oliva-Leyva and G. G. Naumis, Phys. Rev. B **88**, 085430 (2013).
- [34] J. Lee, *Riemannian Manifolds: An introduction to curvature*. (Springer, New York, 1997), 1st ed.
- [35] M. do Carmo, *Differential Geometry of Curves and Surfaces* (Prentice Hall, New Jersey, 1976), 1st ed.
- [36] S. Hollerer and C. C. Celigoj, Comput. Mech. **51**, 765 (2013).
- [37] C. Chen, S. Rosenblatt, K. I. Bolotin, W. Kalb, P. Kim, I. Kymissis, H. L. Stormer, T. F. Heinz and J. Hone, Nature Nano **4**, 861 (2009).
- [38] M. Arroyo and T. Belytschko, Phys. Rev. Lett. **91**, 215505 (2003).
- [39] D.-B. Zhang, E. Akatyeva and T. Dumitrica, Phys. Rev. Lett. **106**, 255503 (2011).
- [40] A. L. Kitt, Z. Qi, S. Rémi, H. S. Park, A. K. Swan and B. B. Goldberg, Nano Lett. **13**, 2605 (2013).

- [41] D. Huertas-Hernando, F. Guinea and A. Brataas, Phys. Rev. B **74**, 155426 (2006).
- [42] A. A. Pacheco Sanjuan, M. Mehboudi, E. O. Harriss, H. Terrones and S. Barraza-Lopez, ACS Nano, DOI: 10.1021/nn406532z. (2014).
- [43] M. Neek-Amal, L. Covaci, K. Shakouri, and F. M. Peeters, Phys. Rev. B **88**, 115428 (2013).
- [44] A. I. Bobenko, P. Schröder, J. M. Sullivan, and G. M. Ziegler, eds., *Discrete Differential Geometry*, vol. 38 of *Oberwolfach Seminars* (Springer, Germany, 2008), 1st ed.
- [45] A. I. Bobenko and Y. B. Suris, *Discrete Differential Geometry: Integrable Structure*. (AMS, USA, 2009), 1st ed.
- [46] Z. Xu and G. Xu, Comp. Math. Appl. **57**, 1187 (2009).
- [47] See supplementary information.
- [48] K. K. Gomes, W. Mar, W. Ko, F. Guinea and H. C. Manoharan, Nature **483**, 306 (2012).
- [49] F. Cirak, M. Ortiz and P. Schröder, Int. J. Numer. Meth. Engng. **47**, 2039 (2000).
- [50] T. Ando, J. Phys. Soc. Jp. **69**, 1757 (2000).
- [51] M. I. Katsnelson. Graphene: Carbon in two dimensions. Cambridge U. Press (2012).
- [52] S.-M. Choi, S.-H. Jhi and Y.-W. Son, Phys. Rev. B **81**, 081407 (2010).
- [53] V. Lukose, R. Shankar and G. Baskaran, Phys. Rev. Lett. **98**, 116802 (2007).
- [54] K.-J. Kim, Ya. M. Blanter and K.-H. Ahn, Phys. Rev. B **84**, 081401(R) (2011); G. M. M. Wakker, R. P. Tiwari and M. Blaauboer, Phys. Rev. B **84**, 195427 (2011).